Prediction of solute rejection and modelling of steady-state concentration polarisation effects in pressure-driven membrane filtration using computational fluid dynamics

Greg Keir* and Veeriah Jegatheesan

School of Engineering, Deakin University, Geelong, Australia

Abstract. A two-dimensional (2D) steady state numerical model of concentration polarisation (CP) phenomena in a membrane channel has been developed using the commercially available computational fluid dynamics (CFD) package CFX (Ansys, Inc., USA). The model incorporates the transmembrane pressure (TMP), axially variable permeate flux, variable diffusivity and viscosity, and osmotic pressure effects. The model has been verified against several benchmark analytical and empirical solutions from the membrane literature. Additionally, the model is able to predict the rejection of an arbitrary solute by the membrane using a pore model, given some basic knowledge of the geometry of the solute molecule or particle, and the membrane pore geometry. This allows for predictive design of membrane systems without experimental determination of the membrane rejection for the specified operating conditions. A demonstration of the model is presented against experimental results for two uncharged test compounds (sucrose and PEG1000) from the literature. The model will be extended to incorporate charge effects, transient simulations, three-dimensional (3D) geometry and turbulent effects in future work.

Keywords: CFD; concentration polarisation; membrane filtration; pore model; predicted rejection

1. Introduction

The pressure-driven membrane processes, including microfiltration (MF), ultrafiltration (UF), nanofiltration (NF), and reverse osmosis (RO), are now widespread industrial processes with significant industrial, economic and environmental importance (Porter 1990). Much research effort has been dedicated to understanding the processes of concentration polarisation (CP) and subsequent membrane fouling, which have limited the efficiency and applicability of these technologies.

Early attempts to characterise CP phenomena were largely based on physical experimentation or empirical models based on simplified solutions of the governing hydrodynamic and mass transfer equations. Examples include the Film Theory Model (Kim *et al*. 2005), the Osmotic Pressure Model (Mulder 1991), and the Boundary Layer Resistance Model (Wijmans *et al*. 1985). In more recent years, approaches based on computational fluid dynamics (CFD) have gained favour as a predictive technique for membrane optimisation and design, with multiple researchers adopting these methods (Geraldes *et al*. 2001, Geraldes *et al*. 2002, Wiley *et al*. 2002, Wiley *et al*. 2003, Fletcher *et al*. 2004). This paper outlines the application of a basic CFD model of the pressure-driven membrane

* Corresponding author, Professor, E-mail: gkeir@deakin.edu.au

processes, focusing on the NF and RO processes, which is to be refined for future work.

2. Modelling

2.1 Model details and solution scheme

A basic representation of the membrane filtration module is used, consisting of a two-dimensional (2D) rectangular membrane feed channel, with one or both walls considered permeable. This configuration is general enough to locally represent a range of membrane geometries for the purpose of investigation of CP effects. The simplification to 2D is justifiable given the low aspect ratio of most membrane feed channels, and is considerably less computationally expensive (Schausberger *et al*. 2009). The software package CFX 13.0 (Ansys, Inc., USA) is used for all simulations of the hydrodynamics of the membrane channel. CFX is a general purpose computational fluid dynamics package, which uses an element-based finite volume method with a co-located grid layout such that the control volumes are identical for all transport equations. A coupled solver is used, where the equations for continuity and momentum are solved simultaneously as a single system (Ansys Inc. 2010).

2.1.1 Geometry

The model consists of a rectangular channel as shown in Fig. 1. The flow through the channel is oriented along the x-axis, and enters at $x = 0$ through the inlet face. The flow exits the channel at $x = L$ through the concentrate face, and permeation occurs through either or both of the lower channel face at $y = -h$, or the upper channel face at $y = h$. The left and right 'walls' of the channel are coupled under the assumption of axisymmetric flow. The right 'wall' of the channel is located at $z = -w/2$, and the left face is located at $z = +w/2$. The width of the channel w (i.e., the thickness of
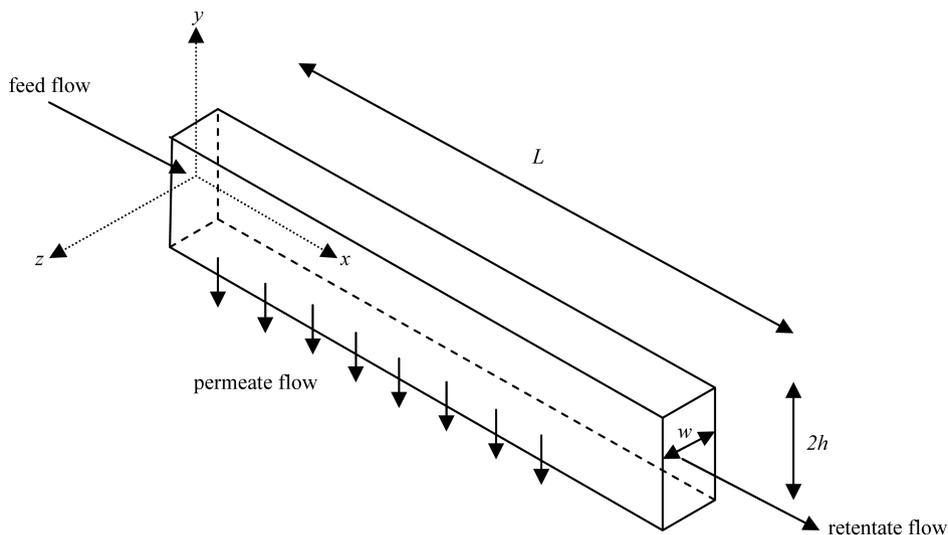

Fig. 1 Model geometry for basic 2D model of laminar flow through porous membrane channel (not to scale)

the single width element) typically should be of the same order as the smallest cell within the face mesh, and was varied as such depending on the face mesh size in later grid dependence studies. While simple rectangular prismatic elements were used for this simple geometry, the model can be generalised to any arbitrary 2D or 3D geometry.

2.1.2 Boundary and initial conditions

Boundary and initial conditions are specified at the channel inlet (in the form of an axial velocity profile) and the channel outlet (as an average static pressure). It is assumed that a fully developed laminar flow profile exists at the channel inlet. The bulk composition of the solution is also specified at the channel inlet in terms of a solute mass fraction for each solute i.

To represent the permeate flow through the membrane, a mass sink is applied at the membrane surface. In this case, at each computational point along the membrane surface a mass sink is applied as the product of the membrane flux as defined by Eq. (1) and the local density of the fluid mixture

$$J_V = L_V(\Delta P - \Delta \Pi_W) \tag{1}$$

where L_V is the hydrodynamic permeability of the membrane and $\Delta\Pi_W$ is the osmotic pressure difference between the feed solution at the membrane surface and the permeate. The TMP is not explicitly applied to the model, as doing so decreases the resolution of small pressure gradients near the membrane surface due to numerical rounding error, as has been noted previously (Fletcher *et al*. 2004). The TMP is instead simply applied as an input parameter to calculate the mass sink expression representing the permeate flux. The solute mass fraction of the permeate is specified at each computational point along the membrane surface according to Eq. (2)

$$\omega_{i,p} = \omega_{i,W}(1 - R_i) \tag{2}$$

where $\omega_{i,p}$ and $\omega_{i,W}$ are the mass fractions of solute i in the permeate stream, and at the membrane surface, respectively, and R_i is the rejection of the solute i. The rejection of a particular solute by a particular membrane is often determined experimentally; however it would be desirable in many cases to predict the solute rejection without recourse to experiment. A method for prediction of the rejections R_i will be considered later in Section 2.4.

A symmetry condition is used for the outer 'walls' of the membrane channel (those parallel to the x-y plane) to allow a 2D simulation. The remaining top and bottom walls of the membrane channel are represented by using standard no-slip boundary conditions in the x-direction, with a mass sink applied to represent the permeation through the membrane surface as discussed previously. The velocity in the y-direction is automatically determined by the CFX solver based upon the local transport properties and the permeate flux imposed by the mass sink term, which is a function of the local solute mass fraction and rejection.

2.2 Computational mesh, convergence and hydrodynamic verification

To ensure the basic hydrodynamics of the membrane channel were correct, the model was first verified for the case where the solute has neutral properties, by which we mean the solution viscosity, density, diffusivity, and osmotic pressure are identical to those of water regardless of the solute concentration. The analytical solutions of Berman (1953) and Karode (2001) where both upper and lower walls of the membrane channel are permeable are used as verification cases for the

model. The model dimensions have been chosen as similar to those used by Karode (2001) for ease of verification. The relevant model input parameters are shown in Table 1. The hydrodynamic behaviour of the model was verified by observing the total axial pressure drop ΔP_{axial} between the membrane inlet and outlet. The axial pressure drop was monitored to ensure that good agreement with the analytical solutions was obtained, and to determine the mesh density at which the calculated pressure drop did not change significantly.

Convergence was observed by monitoring the root mean squared (RMS) residuals for mass, momentum, and solute mass fraction. The model was judged to be converged once all residuals were smaller than 1×10^{-6}. The hydrodynamic model results indicated that good agreement with the analytical solutions was observed using mesh resolutions in the order of 320-640 axial cells (in the x-direction) and 40 vertical cells (in the y-direction). This mesh size was then used as a starting point for later refinement of the mesh which was needed to resolve the fine CP boundary layer. A comparison of the non-dimensionalised axial pressure drop for the converged numerical solution and the analytical solutions is shown in Fig. 2. Excellent agreement is shown between the CFD solution and the analytical solution of Karode (2001); Berman's solution (1953) underpredicts the pressure drop as this solution neglects the axial variation in permeate flux. The axial pressure drop is, of course, lesser than that of an equivalent channel with impermeable walls, shown for comparison.

Table 1 Model input parameters for verification case

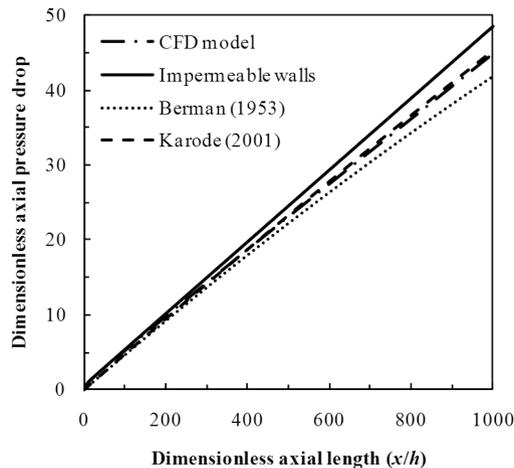| Parameter	Value
Membrane channel length L	1 m
Membrane channel half height h	1 mm
Membrane channel width w	Variable depending on mesh density – equal to size of smallest mesh element
Transmembrane pressure	3 bar
Membrane permeability L_V	9.17×10^{-11} m Pa^{-1} s^{-1}
Inlet Reynolds number N_{Re}	250

Fig. 2 Comparison of dimensionless axial pressure drop for CFD model with analytical solutions for hydrodynamic verification of model

2.3 Incorporation of concentration polarisation effects

Concentration polarisation occurs when rejected solute accumulates next to the membrane surface, forming a boundary layer (Benito *et al.* 1996). This accumulation of solute causes a diffusive flow back to the feed, which eventually reaches a steady-state condition where the solute flow to the membrane surface equals the solute flux through the membrane plus the diffusive flow from the membrane surface back to the feed. The establishment of this boundary layer allows subsequent fouling of the membrane layer to occur; minimisation or removal of the CP layer is thus a primary goal of membrane research.

2.3.1 Spatial variation in transport properties

To describe the effects of concentration polarisation on the permeation of the solute at varying points on the membrane surface, it is necessary for the transport properties of the solution, such as diffusivity, density, and viscosity, to vary spatially over the computational domain as a function of solute concentration A simple approach and test case was derived from the work of Geraldes *et al.* (2001) in which the viscosity, diffusivity and osmotic pressure of aqueous solutions of several compounds are described as polynomial functions of the solute mass fraction. The two uncharged compounds used in this study (sucrose and PEG1000) have been used as test compounds for the present model.

The solution density cannot be explicitly specified as a function of the solute mass fractions due to software limitations, but is calculated using a harmonic average based on the density of the individual components within the solution. The osmotic pressure is calculated as an additional scalar parameter which varies across the solution domain as a function of the solute mass fraction, and is then used to determine a more accurate approximation of the permeate flux at the membrane surface as per Eq. (1). The relevant expressions are shown in Table 2.

2.3.2 Mesh refinement for resolution of CP layer

Significant mesh refinement is required in the vicinity of the membrane surface to adequately resolve the fine CP boundary layer. Previous hydrodynamic models had indicated cell aspect ratios of roughly $30 - 60$ gave acceptable results. This was used as a starting point for a grid independence study using the geometry of Geraldes *et al.* (2001), which is shown in Table 3. The vertical mesh resolution and the degree of refinement near the membrane surface were both investigated in the grid independence study. The final mesh configuration chosen was that of 100 axial cells by 75 vertical cells, with the mesh size varying in the vertical direction such that the height of the largest mesh cell (in the centre of the channel) was 100 times that of the smallest mesh cell (adjacent to the membrane wall).

In addition, initial model runs indicated that additional refinement was necessary at the channel

Table 2 Trial solute components and expressions for transport properties (after (Geraldes *et al.* 2001))

Compound	Density ρ (g cm^{-3})*	Viscosity $\mu \times 10^3$ (Pa s)	Diffusivity $D \times 10^9$ (m^2 s^{-1})	Osmotic pressure $\Pi \times 10^{-5}$ (Pa)
Sucrose	1.587	$0.89(1 + 1.31\omega_i + 16.83\omega_i^2)$	$0.52(1 - 1.33\omega_i)$	$72.18\omega_i(1 + 0.94\omega_i + 2.93\omega_i^2)$
PEG1000	1.12	$0.89(1 + 6.59\omega_i + 120.8\omega_i^3)$	0.309	$24.64\omega_i(1 + 2.94\omega_i + 19.25\omega_i^2)$

* Used for CFX internal calculation of solution density using harmonic average

Table 3 Model input parameters for simulations corresponding with Geraldes *et al.* (2001)

Parameter	Value
Membrane channel length L	200m m
Membrane channel half height h	1 mm
Membrane channel width w	Variable depending on mesh density – equal to size of smallest mesh element
Transmembrane pressure	1, 2, 3, 4 MPa
Membrane permeability L_V	1.4 x 10^{-11} m Pa^{-1} s^{-1}
Inlet Reynolds number N_{Re}	500, 2000

inlet to smoothly describe the 'leading edge' of the CP boundary layer. The mesh was refined so that the first cells at the inlet were of unity aspect ratio, growing progressively larger along the *x*-axis until $x = 10$ mm, after which point the cells were of equal length for the remainder of the channel.

2.4 Solute rejection prediction using extended Nernst-Planck equation

A difficulty in constructing predictive models of membrane CP and fouling is determination of the rejection factor of the membrane for a particular solute or pollutant. This is typically achieved by experimental measurement of a laboratory scale model of the membrane-solute combination in question. Clearly this is not always desirable or economic to do so.

The extended Nernst-Planck equation can be used to describe the transport of solutes through a membrane (Bowen *et al.* 1996, Bowen *et al.* 1997), and hence predict the rejection of a solute by a membrane based on several physically meaningful parameters. It can be written as shown in Eq. (3), where the terms on the right hand side represent diffusion, convection, and in the case of a charged solute, electric migration, respectively, for some solute *i*

$$j_i = -K_{i,d}D_i\frac{dc_i}{dy} + K_{i,c}c_iJ_V - \frac{z_ic_iK_{i,d}D_i}{RT}F\frac{d\psi}{dy} \tag{3}$$

where j_i is the solute flux, D_i is the bulk diffusivity, z_i is the electrical valence, and c_i is the concentration inside the membrane. The terms $K_{i,c}$ and $K_{i,d}$ represent the hindered convection and diffusion of the solute inside the membrane, respectively: the determination of these terms will be considered later. The overall volumetric flux through the membrane is given by J_V, and y is the axial coordinate along the direction of the solution flux. The final term on the right hand side of Eq. (3) representing transport due to electric migration depends on the Faraday constant F, the ideal gas constant R, the absolute temperature T, and the electric potential ψ. In the case of an uncharged solute, the electric migration term in Eq. (3) disappears to give

$$j_i = -K_{i,d}D_i\frac{dc_i}{dy} + K_{i,c}c_iJ_V \tag{4}$$

We assume that the rejection of the uncharged solute can be modelled by a steric partitioning coefficient Φ which describes the accessibility of the pore to the solute. The determination of the steric partitioning coefficient will be considered later. This applies at the interface between the membrane and the external solution both at the pore inlet ($y = 0$) and pore outlet ($y = \Delta y$), such that

$$c_{i,y=0} = \Phi C_{i,W} \tag{5}$$

$$c_{i,y=\Delta y} = \Phi C_{i,p} \tag{6}$$

where c_i is the concentration inside the membrane, C_i is the concentration of the external solution, and the subscripts W and p represent the feed solution adjacent to the membrane wall, and the permeate solution, respectively. The solution concentration adjacent to the membrane wall $C_{i,W}$ is obtained from the solution of the CFD model, incorporating the spatially variable solute concentrations and associated transport properties, and hence includes the effects of concentration polarisation on the feed side of the membrane. By writing the flux of solute i as $j_i = J_V C_{i,p}$, an analytical expression for the rejection can be obtained

$$R_i = 1 - \frac{C_{i,p}}{C_{i,W}} = 1 - \frac{\Phi K_{i,c}}{1 - (1 - \Phi K_{i,c})\exp(K_{i,c}J_V \Delta y / K_{i,d}D_i)} \tag{7}$$

2.4.1 Steric partition effects

The steric partitioning coefficient Φ describes the rejection of the solute due to steric (molecular sieving) effects. These so-called steric pore flow models have typically been used to describe the behaviour of NF and UF membranes, but are in principle capable of describing rejection due to sieving effects for RO and MF membranes as well, though such effects may be less important for MF due to the large pore sizes, and the assumption of well-defined, discrete pores may not be accurate for RO membranes. Nevertheless, such models provide a promising general approach to describing rejection for the pressure-driven membrane processes.

The simplest method for describing steric effects is to assume a spherical solute, which is sound in the case for most ionic solutes and small molecular solutes. The partitioning coefficient can then be written as a function of the membrane pore radius r_p and the solute radius, typically approximated as the Stokes radius, r_s

$$\Phi = (1-\lambda)^2, \ \lambda = r_s/r_p \tag{8}$$

Eq. (8) is of course applicable only for $\lambda \leq 1$; for $\lambda > 1$, the partitioning coefficient is set to zero and hence the rejection becomes unity. For larger solutes, the shape of the solute plays an important role in the steric interactions between the pore and solute. A method for determining the steric partitioning coefficient Φ for a non-spherical solute was described by Kiso *et al*. (2001, 2010, 2011), and has been adopted in the present model. The method is described briefly in the following.

Approximating the solute as a rectangular parallelepiped, the solute length L_S is given by the distance between the two most distant points on the solute (effectively the distance between the two most distant atoms in the molecule inclusive of the Van der Waals radius). The line that joins these two most distant points is defined as the L-axis. The solute width is determined by projecting the solute particle onto the plane perpendicular to the L-axis, and constructing the smallest possible rectangle on that plane which will fully enclose the projection of the solute particle. Defining the area of this rectangle as S, the particle width W_S can then be calculated

$$W_s = \frac{1}{2}\sqrt{S} \tag{9}$$

As the solute particles are considered to be non-spherical, the solute orientation affects the

proportion of the pore area that is accessible to the solute. The length of the projection of the solute against the pore surface is called the effective solute length, and is given by

$$L_p = L_S \cos\alpha + 2W_S \sin\alpha \tag{10}$$

where the angle between the L-axis and the pore surface is α. The steric partition factor for some angle α is thus given by

$$\Phi(\alpha) = \left(\frac{a}{r_p}\right)^2 \tag{11}$$

$$a = \sqrt{r_p^2 - \left(\frac{L_p}{2}\right)^2} - W_S \tag{12}$$

A probabilistic approach is used to calculate an overall partition coefficient Φ as follows

$$\Phi = \int_0^{\pi/2} \Phi(\alpha)p(\alpha)d\alpha \tag{13}$$

$$\int_0^{\pi/2} p(\alpha)d\alpha = 1 \tag{14}$$

where the probability function $p(\alpha)$, representing the probability of an individual solute being oriented at an angle α and chosen to satisfy Eq. (14), is $p(\alpha) = \sin(\alpha)$. Other probability functions that satisfy Eq. (14) may of course be chosen; the function used here is that determined by Kiso *et al.* (2010) to give the best agreement with experimental data for a range of uncharged compounds.

For solutes on the molecular scale, semi-empirical techniques are available to predict molecular geometry, such as the MOPAC2009 software (Stewart Computational Chemistry, CO, USA), which has been adopted for the compounds used in this study. In principle, this approach could also be adopted for larger particular pollutants (as in MF processes), as long as an estimation of the particle geometry can be made.

2.4.2 Calculation of hindrance factors
The hindrance factors for diffusion (K_d) and convection (K_c) are also functions of the ratio of the solute radius to pore radius, λ. Here, the expressions presented by Bowen *et al.* (1997) have been used

$$K_d = 1.0 - 2.30\lambda + 1.154\lambda^2 + 0.224\lambda^3 \tag{15}$$

$$K_c = (2 - \Phi)(1.0 + 0.054\lambda - 0.988\lambda^2 + 0.441\lambda^3) \tag{16}$$

2.4.3 Volumetric flux approximation
In Eq. (7), the rejection depends on the volume flux J_V which is unknown. The flux could be determined using the Hagen-Poiseuille equation, though this requires knowledge of the osmotic pressure difference between the feed and permeate. As the rejection is still unknown, the permeate osmotic pressure is also unknown without experimental measurement. For this work it was decided that a reasonable approximation was to assume that the osmotic pressure in the permeate stream

was zero, though only for the purpose of determining the approximate water flux $J_{v,approx}$ in order to approximate the rejection factor. That is, the transmembrane osmotic pressure difference is approximated by the local osmotic pressure at the membrane surface Π_W only, as per Eq. (17)

$$J_{v,approx} = \frac{r_p^2(\Delta P - \Pi_W)}{8\,\eta\Delta y}$$

(17)

where ΔP is the transmembrane pressure (TMP), and η is the viscosity of the water in the pore. The approximate water flux $J_{v,approx}$ is then used in place of J_V in Eq. (7). In this approach, the membrane porosity is not used, and is implicitly included in the chosen value for the pore length Δy to maintain consistency with the approach presented by Kiso *et al*. (2010, 2011).

It is stressed that this flux is used only for calculation of the rejection coefficient of the solute, and does not determine the magnitude of the mass sink (permeate flux) applied as a boundary condition to the hydrodynamic model. Full osmotic pressure effects are still included in the hydrodynamic model and in determining the permeate flux through the membrane. However, a benefit of this approach is that the rejection of the solute by the membrane may vary spatially across the membrane surface depending on the hydrodynamic solution.

2.4.4 Determination of membrane parameters

The only parameter thus needed to predict the rejection for a solution containing uncharged solutes and an arbitrary membrane is the membrane pore radius r_P. In principle the pore radius can be determined by inspection of the membrane via methods such as atomic force microscopy (e.g. Bowen *et al*. 1997). However, in practice, typically experimental measurement of the rejection of a single uncharged solute is made, and the pore radius is then adjusted to achieve good agreement with the experimentally measured rejection. The pore length Δy is technically not necessary to predict the rejection (i.e., Eq. (7) does not depend on the pore length), but it can be used if an estimation of the permeate flux is desired, with the volumetric flux written as

$$J_v = \frac{r_p^2(\Delta P - \Delta\Pi_W)}{8\,\eta(\Delta y/A_k)}$$

(18)

where A_k is the membrane porosity. Eq. (18) is thus essentially equivalent to Eq. (1), and could be used as such if the membrane porosity and pore length are known.

In this case, it is unnecessary to do so as the hydrodynamic permeability of the membrane is known and the permeability is not, but the pore length parameter has been retained for future use in the model in the case of charged solutes, where a solution of the full extended Nernst-Planck equation (Eq. (3)) is required.

3. Simulations

Simulations were run for the conditions described previously in two main trials: firstly, using the rejection factors determined experimentally by Geraldes *et al*. (2001), and then using the rejection factors predicted using the pore model described in Section 2.4.1. All simulations were run using a solute feed mass fraction of 0.002 kg kg^{-1}.

3.1 Simulations using experimentally determined rejection

The experimental data from Geraldes *et al*. (2001) was used to provide the membrane rejection factors for each solute at varying transmembrane pressures, which are shown in Table 4. The membrane used in these experiments was the CDNF50l thin-film composite NF membrane (supplied by Separem, Biela, Italy), with a measured hydrodynamic permeability of 1.4×10^{-11} m^2 s kg^{-1}. Experiments were conducted at several different crossflow velocities; the data used for this study are for the extreme values (the lowest and highest studied velocities), which are equivalent to entrance Reynolds numbers ($N_{Re} = 4u_0h\rho/\eta$) of 500 and 2000, respectively. These are equivalent to the stated Reynolds numbers of 250 and 1000 given by Geraldes *et al*. (2001) due to a different formulation of the entrance Reynolds number – the formulation used here is consistent with Berman (1953) and Karode (2001). The rejection values given were measured for the case where $N_{Re} = 2000$.

A comparison of the permeate fluxes predicted by the current model and the experimental flux data and model results of Geraldes *et al*. (2001) is shown in Fig. 3. Values were compared at three collector sites (Collectors 1, 2 and 3) located 7.5 mm, 22.5 mm and 45 mm from the channel inlet, respectively. Reasonable agreement with the experimentally determined flux values is shown, though the model consistently overpredicts the permeate flux. However, the current model generally gives better agreement with the experimentally determined fluxes than the model results of Geraldes *et al*. (2001), probably due to the increased spatial resolution of the current model.

The ability of the model to predict the formation of the CP boundary layer was evaluated by comparing the predicted non-dimensional CP boundary layer profiles with those presented by Geraldes *et al*. (2001). The non-dimensionalised CP boundary layer height δ_W/h is plotted as a function of the dimensionless axial length x/h in Fig. 4. The profiles show good agreement with those determined by Geraldes *et al*. (2001). As expected, a higher entrance Reynolds number corresponds to a thinner CP boundary layer, due to increased shear disrupting the CP boundary layer.

3.1.1 Osmotic pressure correction factor

The model consistently overpredicts the permeate flux compared to the experimentally determined flux values. An attempt was made by Geraldes *et al*. (2001) to compensate for this over-prediction of flux by use of an osmotic pressure correction factor Λ, where the corrected permeate flux is given by

Table 4 Predicted and experimentally observed rejection factors for test compounds for CDNF50l thin-film composite NF membrane (Separem, Biela, Italy)

Compound	Transmembrane pressure ΔP							
	1 MPa		2 MPa		3 MPa		4 MPa	
	R_{obs}*	R_{cal} [†]	R_{obs}	R_{cal}	R_{obs}	R_{cal}	R_{obs}	R_{cal}
Sucrose	0.993	0.993 0.993	0.996	0.993 0.993	0.998	0.993 0.993	0.999	0.993 0.993
PEG1000	0.9981	1.000 1.000	0.9987	1.000 1.000	0.9993	1.000 1.000	0.9995	1.000 1.000

* Observed rejection data from (Geraldes *et al*. 2001) for $N_{Re} = 2000$
[†] Calculated rejection data averaged over membrane surface using pore model derived from (Kiso *et al*. 2011) with pore size of 0.79 nm for $N_{Re} = 500$ and $N_{Re} = 2000$, respectively
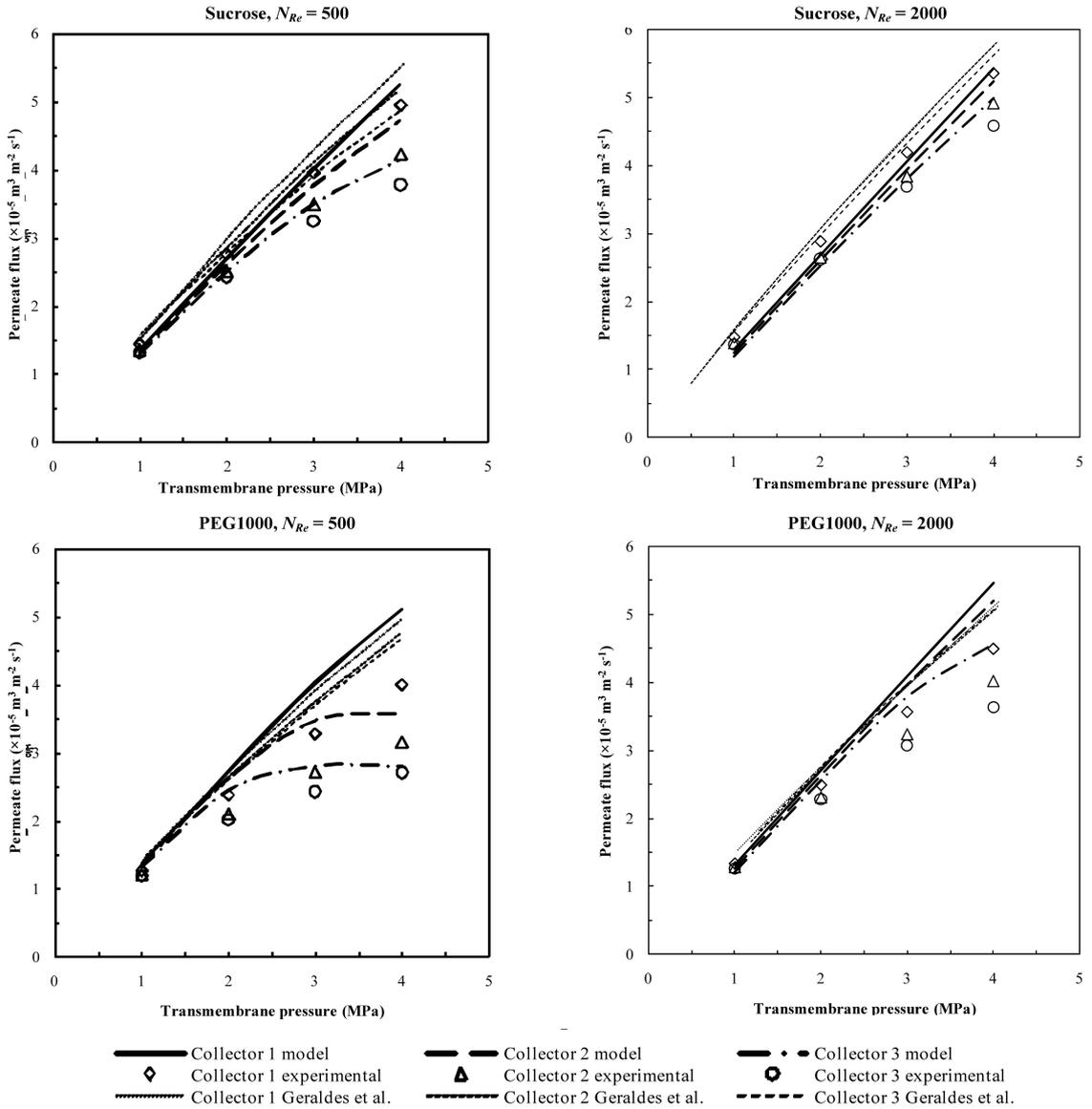
Fig. 3 Comparison of predicted permeate fluxes for CFD model with experimental and modelled fluxes from (Geraldes *et al*. 2001) using experimentally determined rejection factors

$$J_V = \varLambda L_V(\Delta P - \Delta\Pi_W) \tag{19}$$

To see if this approach would account for the flux discrepancy in the current model, a set of simulations was carried out using the osmotic correction approach with expressions for $\varLambda$ as a function of the solute mass fraction as given by Geraldes *et al*. (2001), which are shown in Table 5. The permeate fluxes and CP boundary layer profiles obtained from these simulations are shown in Figs. 5 and 6, respectively. The overall agreement with the experimental flux values, when averaged
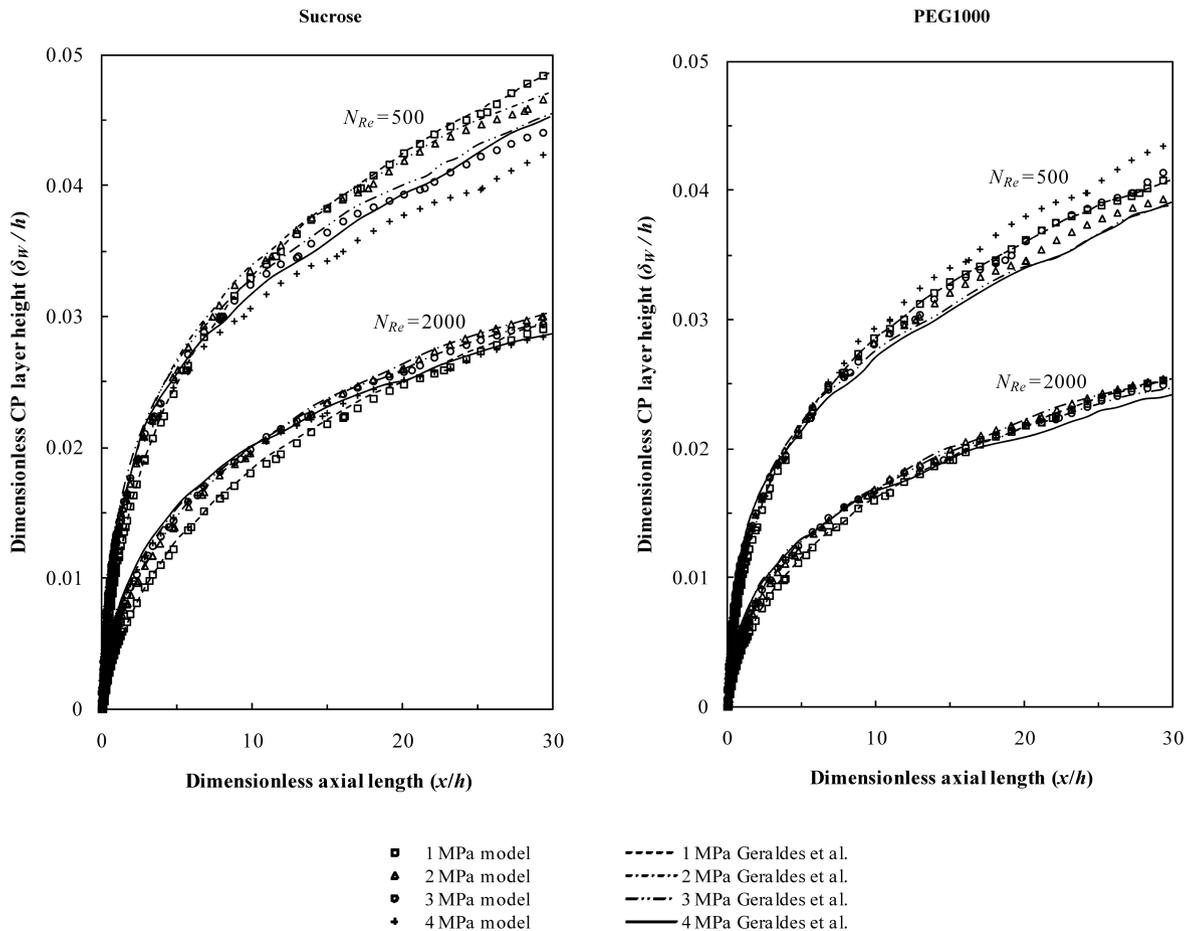
Sucrose   **PEG1000**

Fig. 4 Comparison of dimensionless CP boundary layer profile for CFD model with computational results of (Geraldes *et al*. 2001) using experimentally determined rejection factors

Table 5 Osmotic pressure correction factor expressions for test compounds (after (Geraldes *et al*. 2001))

Compound	Osmotic pressure correction factor Λ *
Sucrose	$1 - 0.375(1000 \, \omega_i)^{0.4}$
PEG1000	$1 - 0.0384 (1000 \, \omega_i)^{0.31}$

* Expressions have been modified to account for different units for solute mass fraction

over all combinations of transmembrane pressure and collector location, is improved for PEG1000 for both inlet Reynolds numbers. However, the overall agreement is actually decreased for sucrose for both Reynolds numbers, where the model tends to underpredict the flux, especially at higher transmembrane pressures. In all cases, however, the model's flux predictions are significantly closer to the experimental results than the model results of Geraldes *et al*. (2001), again probably a function of the increased spatial resolution of the current model. The modelled CP boundary layer profiles remain largely identical to those obtained without the osmotic pressure correction factor.
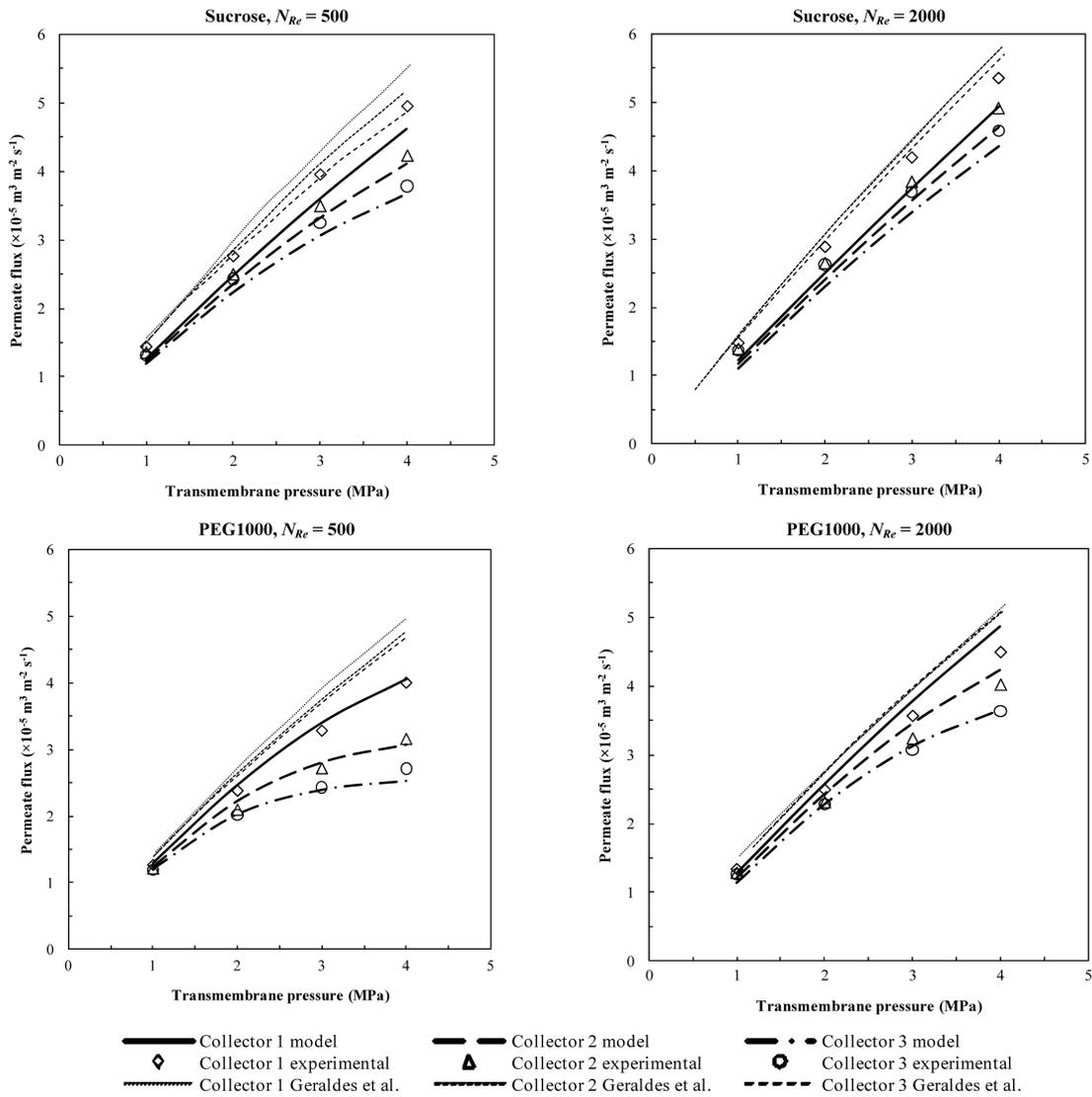
Fig. 5 Comparison of predicted permeate fluxes for CFD model incorporating osmotic pressure correction factor with experimental and modelled fluxes from (Geraldes *et al*. 2001) using experimentally determined rejection factors

3.2 Simulations using predicted rejection from pore model

The experimental data from Geraldes *et al*. (2001) was used to test the accuracy of the pore model described previously in predicting the rejection factor. The MOPAC2009 software was used to predict the solute molecule geometry for the two test compounds as shown in Table 6. For all simulations, an osmotic pressure correction factor was not used, in order to properly elucidate the effect of the spatially variable rejection model on the predicted permeate fluxes, if any.

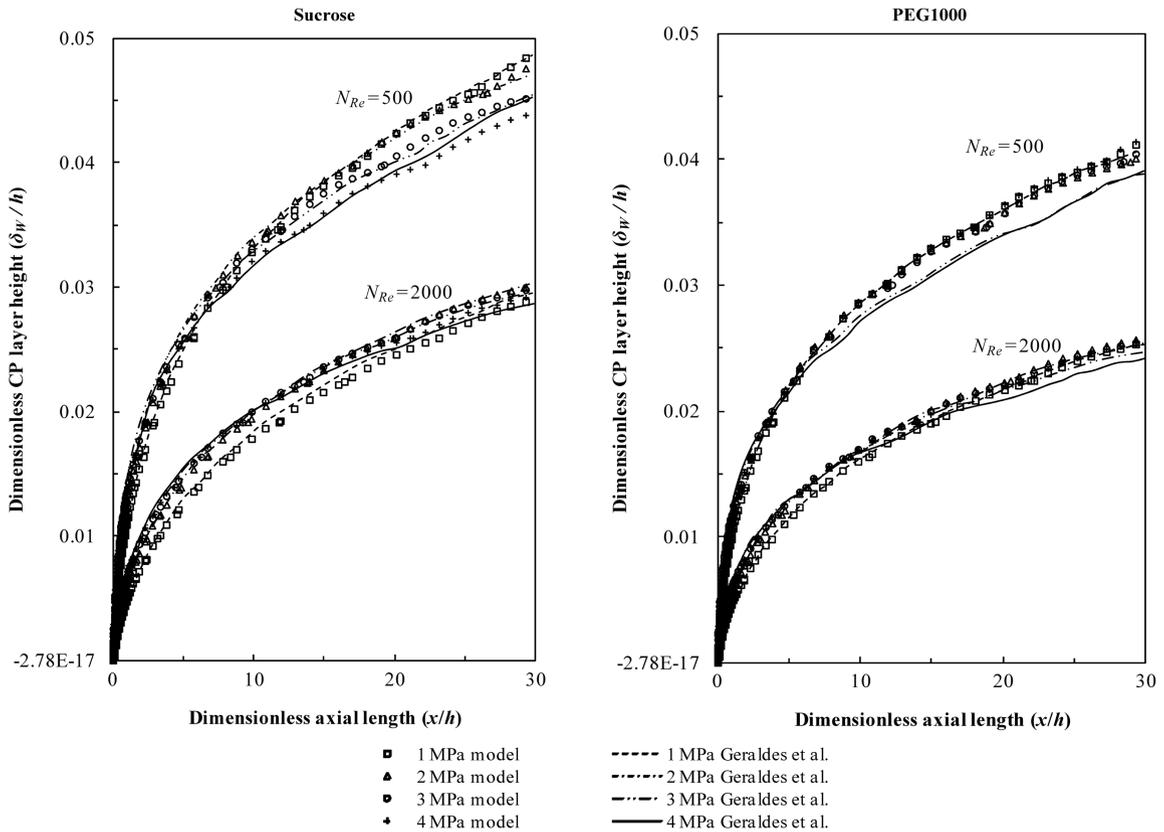Detailed information on the geometric properties of the CDNF50l membrane was unavailable;

Fig. 6 Comparison of dimensionless CP boundary layer profile for CFD model incorporating osmotic pressure correction factor with computational results of (Geraldes *et al*. 2001) using experimentally determined rejection factors

Table 6 Molecular properties for test compounds derived using MOPAC2009 software

Compound	Molecular formula	Molecular weight (g mol^{-1})	Solute length L_S (nm)	Solute width W_S (nm)
Sucrose	$C_{12}H_{22}O_{11}$	342.30	0.973	0.480
PEG1000	H-$(OCH_2CH_2)_n$-OH*	~ 1000	5.459	1.549

* Generic formula for polyethylene glycol – here n = 22 to correspond with listed average molecular weight of 1000 g mol^{-1}

however de Pinho *et al*. (2002) performed a series of experiments in which the average pore radius for this membrane was characterised as 0.52 nm. This value was obtained by comparing results from a similar pore model, assuming a spherical molecule, and experimental studies. Using a similar approach, a pore radius of 0.79 nm gave good agreement with the experimentally measured rejection factors for the present non-spherical model. As the rejection in the current formulation can vary axially with the local osmotic pressure and TMP, which depends on the hydrodynamic solution, a representative rejection value averaged over the membrane surface was compared against the

measured rejection in order to determine the pore radius. This was done for $N_{Re} = 2000$ to correspond with the experimental conditions under which the rejection was measured by Geraldes *et al.* (2001).

That the use of a non-spherical model yields a larger apparent pore radius than a spherical pore model is a fairly obvious result, which is consistent with other results in the literature (Kiso *et al.* 2010, Kiso *et al.* 2011). In addition, the ratio of the calculated pore radius for the spherical model to the non-spherical model (~0.6) is similar to that obtained by Kiso *et al.* (2010, 2011). If the Hagen-Poiseuille equation is used to predict the pure water flux through the membrane with an assumed porosity of 0.1 as per Kiso *et al.* (2011), a pore length of 8.9×10^{-8} m yields the same hydrodynamic
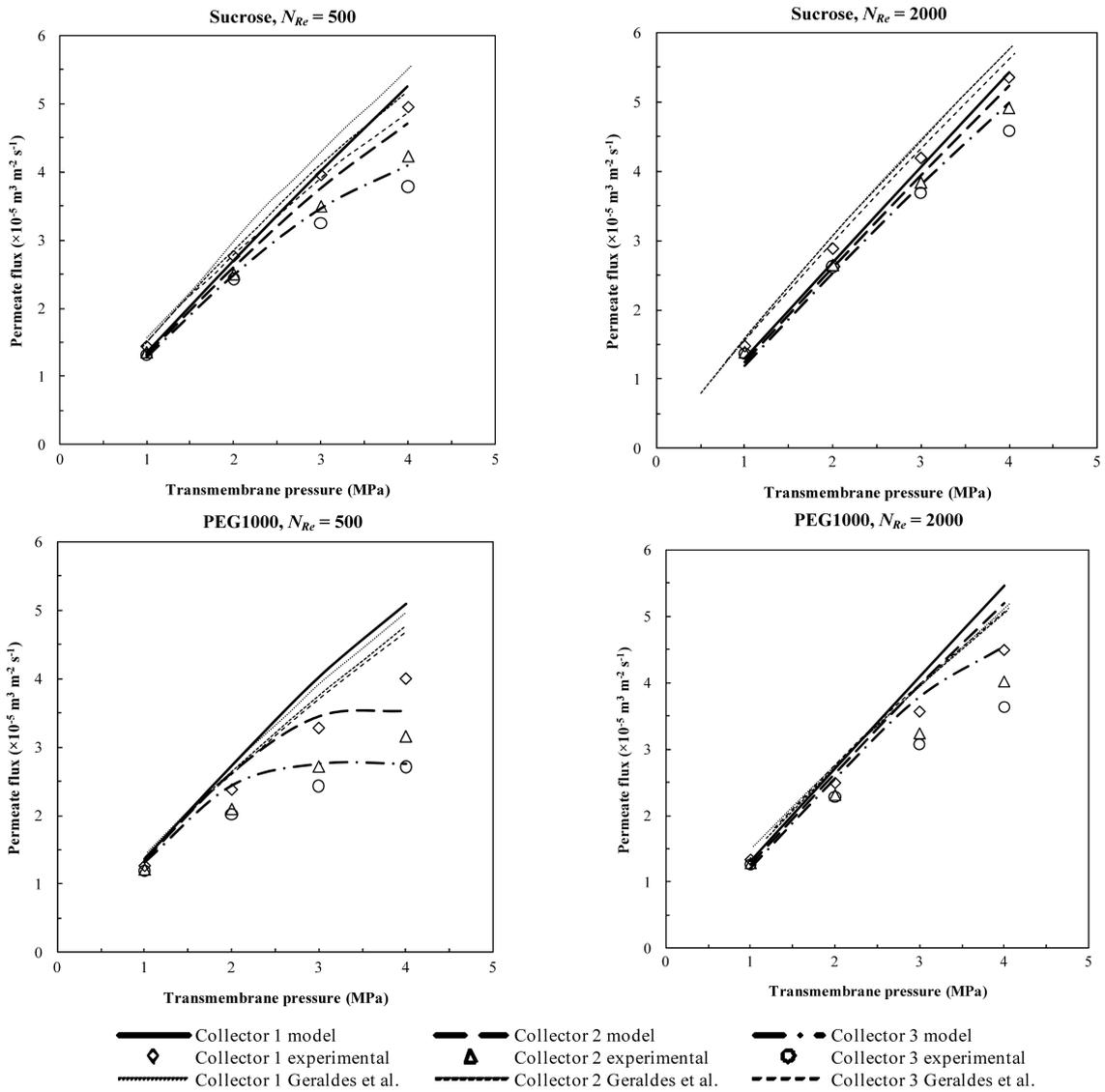

Fig. 7 Comparison of predicted permeate fluxes for CFD model with experimentally determined fluxes of (Geraldes *et al.* 2001) using calculated spatially varying rejection factors from pore model

permeability as measured by Geraldes *et al*. (2001). This is broadly consistent with other stated pore lengths in the literature (e.g., Kiso *et al*. 2011).

The rejection factors calculated by the pore model in conjunction with the hydrodynamic model are shown in Table 4. Rejection values shown are averaged over the membrane surface for both inlet Reynolds numbers, using the pore radius of 0.79 nm determined using the experimental data for the higher inlet Reynolds number of $N_{Re} = 2000$. Good agreement is shown between the experimentally determined rejection factors and the averaged values obtained through the present model. For PEG1000, the modelled molecular dimensions are sufficiently large to ensure complete rejection along the entire axial length (that is, the modelled molecular shape is larger than the entrance to the membrane pores regardless of its orientation). The experimental rejection data indicates that PEG1000 should have rejection slightly less than unity, which suggests that either the modelled molecular shape is too large; or, more likely, that there is some variability in pore size within the membrane so that a small proportion of solute is permitted through the larger pores. This issue can be addressed with the use of a pore size distribution rather than a uniform pore size to represent the porous membrane structure as described by Kiso *et al*. (2010), which will be included in future work. The axial variation in rejection for both compounds is largely negligible, as the variation in osmotic pressure and hydrodynamic pressure is small compared to the applied TMP for
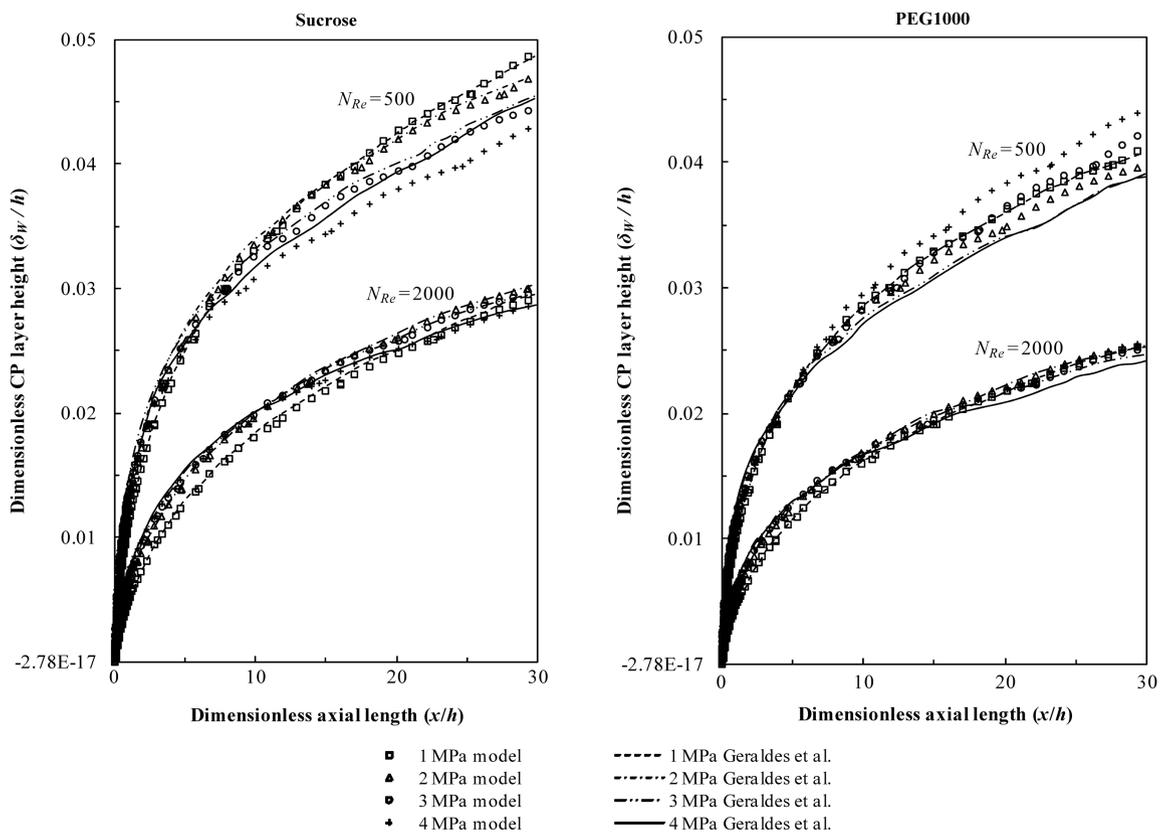

Fig. 8 Comparison of dimensionless CP boundary layer profile for CFD model with computational results of (Geraldes *et al*. 2001) using calculated spatially varying rejection factors from pore model

the test cases.

The permeate fluxes obtained from these simulations are shown in Fig. 7. The modelled permeate fluxes are almost identical to those obtained using a constant experimentally obtained rejection factor as in Fig. 3. As well, the predicted CP boundary layer profiles, shown in Fig. 8, are largely identical to those obtained with the experimental rejection factors (Fig. 4).

3.3 Simulations using predicted rejection from pore model for low transmembrane pressure

To see if the axial variation in rejection would have any effect on fluxes or CP layer thicknesses, a trial was conducted only for a lower range of TMPs (0.125 – 0.5 MPa), using both an axially varying rejection, and a constant rejection obtained from the average of the prior simulation. This exercise has been performed for the sucrose solution only, as the modelled pore dimensions ensure complete rejection of PEG1000 regardless of TMP. For this case, the axial variation in rejection is shown in Fig. 9 as a function of the non-dimensional axial length. The predicted rejection decreases along the channel length, as the osmotic pressure increases and the hydrodynamic pressure decreases. No results are shown for the higher Reynolds number case for the TMPs of 0.125 MPa
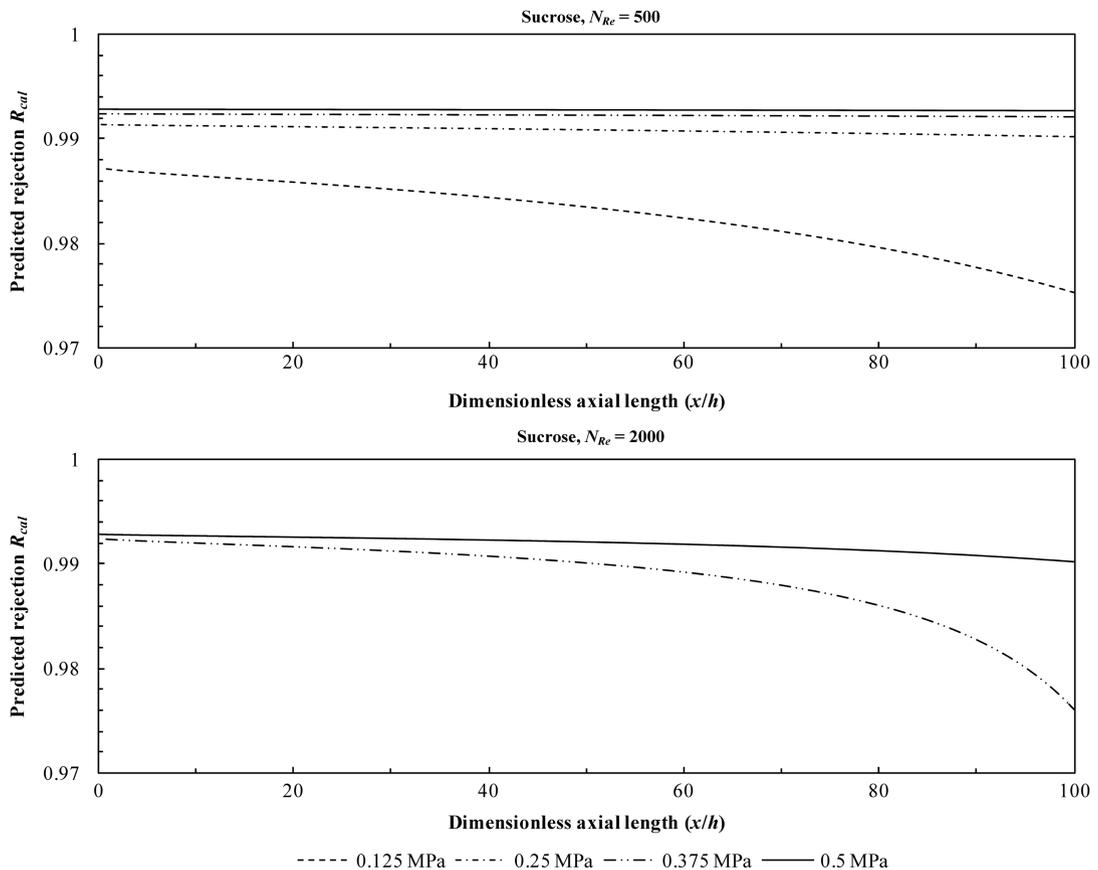

Fig. 9 Axial variation in sucrose rejection for low transmembrane pressure with spatially varying rejection factor

and 0.25 MPa, as the osmotic pressure in these cases is large enough to preclude positive flux through the membrane.

Comparisons of the predicted membrane fluxes and CP layer profiles for the low TMP cases are shown in Figs. 10 and 11, respectively. The predicted CP layer profiles and fluxes are identical whether the rejection is varying or constant, primarily due to the very small variations in rejection as shown in Fig. 9. However, if conditions were such that the axial rejection variation were greater, it might be expected that the predicted CP layer thickness for the varying rejection simulation is slightly decreased compared to the constant rejection. The discrepancy in CP layer thickness would presumably grow larger as the axial distance increases: as the rejection factor decreases along the channel length, the hydrodynamic pressure decreases and osmotic pressure increases. Consequently, as more solute is permitted through the membrane at increasing axial lengths, the solute concentration at the membrane surface and hence the height of the CP boundary layer would, in theory, decrease. Similarly, one might expect a slight decrease in the modelled fluxes when the rejection is allowed to vary, which becomes more significant as the axial distance along the membrane channel increases, though this is not observed for the conditions modelled here.

The inability of the spatially variable rejection factor to address the discrepancy between modelled and experimentally measured fluxes suggests that further mechanisms not included in the current model may be operating to reduce the flux, separate from any variation in the intrinsic rejection of the membrane. Determining the nature of these mechanisms and quantifying how they may be represented without resorting to the empirical approach of the osmotic pressure correction factor may be a useful direction of investigation for future work.
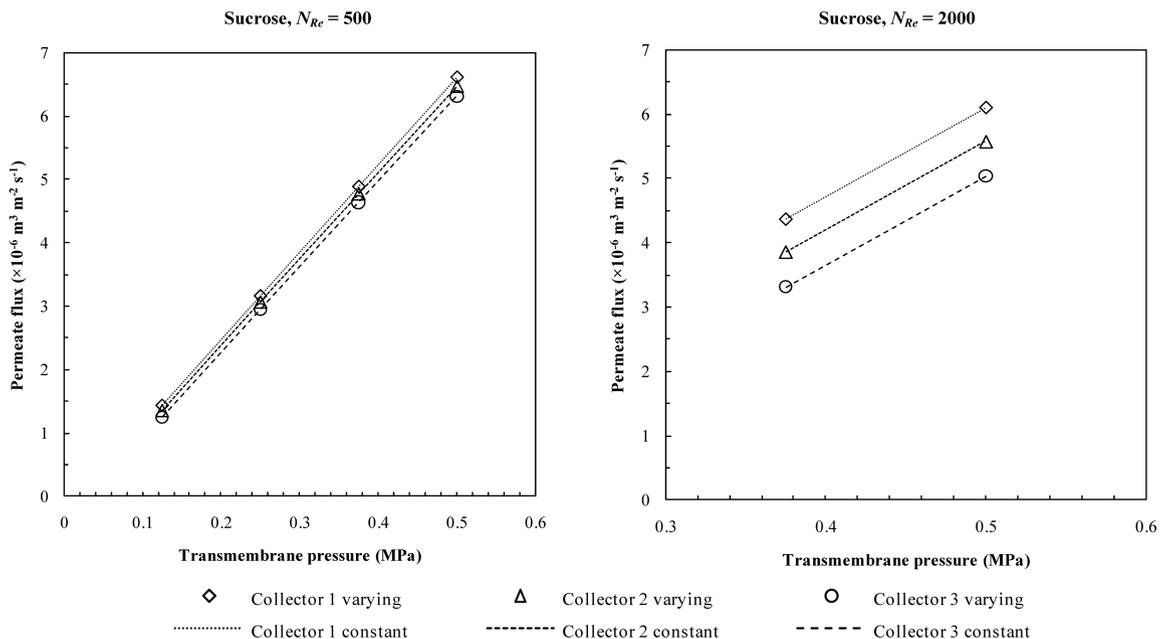

Fig. 10 Comparison of predicted permeate fluxes for CFD model for low transmembrane pressures using calculated constant and spatially varying rejection factors
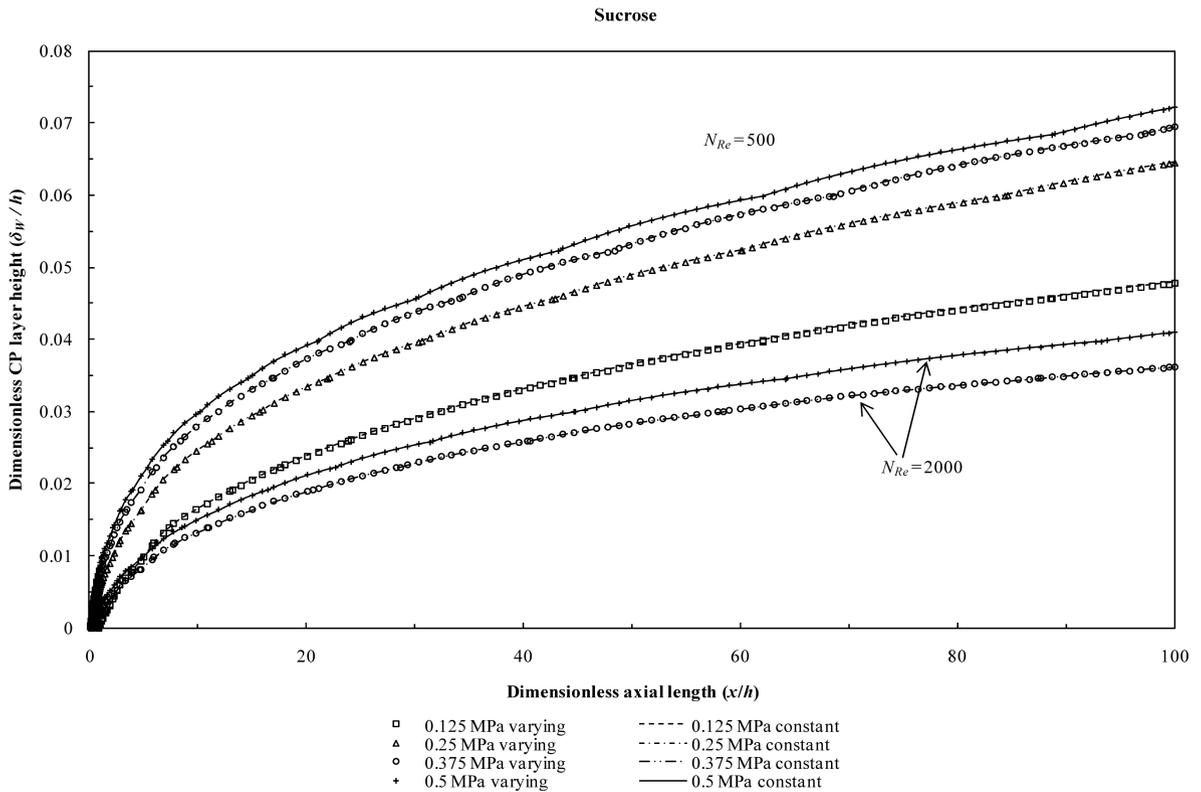
Sucrose

Fig. 11 Comparison of dimensionless CP boundary layer profile for CFD model for low transmembrane pressures using calculated constant and spatially varying rejection factors

4. Conclusions

The CFD model and associated predictive rejection pore model presented here allow for *a priori* prediction of the membrane flux and CP boundary layer profile for an arbitrary membrane-uncharged solute combination, provided the geometric characteristics of the solute and membrane pores are known. In addition, the model allows for the rejection of the solute by the membrane to vary spatially within the membrane channel as a function of the local hydrodynamic conditions, though this does not seem to have any significant effects on flux or CP layer profiles for the conditions tested here. Good agreement is obtained between the predicted permeate flux and experimentally observed flux. The results also indicate that use of an artificial osmotic correction factor to rectify the often observed discrepancy between predicted and measured flux provides even better agreement in most cases, though the mechanisms of flux reduction that the correction factor empirically represents have yet to be elucidated fully. The CP boundary layer profiles predicted by the model match well with those predicted by other models in the literature.

The model can be considered applicable for membrane-solute systems where concentration polarisation occurs, and where the primary mechanism of solute removal is by steric or sieving effects, i.e. where the solute is of the same order of size as the membrane pore radius. To extend the applicability of the model to such systems, other phenomena and removal mechanisms must be

incorporated. The present approach can be extended to include charge effects by a full solution of the extended Nernst-Planck equations using a Donnan equilibrium approach to describe the electric migration of solutes, which is being implemented within the model for future work. In addition, description of other effects such as cake formation would be desirable.

It is also recognised that membrane fouling is an inherently transient process, and the method presented here for prediction of rejection is an approximation to determine the initial rejection for a membrane without concentration polarisation. It is intended to extend the rejection model in future work in conjunction with a transient hydrodynamic model to allow for the rejection to vary as a function of filtration time, where the estimated rejection can be refined with each time step by an updated estimate using the hydrodynamic solution for the previous time step. Additionally, the model should allow for the build up of solute within the membrane pore over time to more accurately simulate physical pore blocking effects, as well as allowing for variable pore sizes or a pore size distribution.

Finally, many membrane modules have significantly more complex geometry than the simple case considered here, and turbulent effects may also be important in some processes. It is intended that future work will extend the basic model presented here so that a more general computational model of the membrane fouling process can be realised.

Acknowledgements

References

(2010). *ANSYS CFX-Solver Theory Guide*, Canonsburg, PA, ANSYS, Inc.

Benito, J.M. and Richard, I.U. (1996), "Modeling concentration-polarization in reverse osmosis spiral-wound elements", *J. Environ. Eng.*, **122**(4), 292-298.

Berman, A.S. (1953), "Laminar flow in channels with porous walls", *J. Appl. Phys.*, **24**(9), 1232-1235.

Bowen, W.R., Mohammad, A.W. and Hilal, N. (1997), "Characterisation of nanofiltration membranes for predictive purposes -- use of salts, uncharged solutes and atomic force microscopy", *J. Membrane Sci.*, **126**(1), 91-105.

Bowen, W.R. and Mukhtar, H. (1996), "Characterisation and prediction of separation performance of nanofiltration membranes", *J. Membrane Sci.*, **112**(2), 263-274.

de Pinho, M.N., Semião, V. and Geraldes, V. (2002). "Integrated modeling of transport processes in fluid/ nanofiltration membrane systems", *J. Membrane Sci.*, **206**(1-2), 189-200.

Fletcher, D.F. and Wiley, D.E. (2004), "A computational fluids dynamics study of buoyancy effects in reverse osmosis", *J. Membrane Sci.*, **245**(1-2), 175-181.

Geraldes, V., Semião, V. and Pinho, M.N.D. (2001), "Flow and mass transfer modelling of nanofiltration", *J. Membrane Sci.*, **191**(1-2), 109-128.

Geraldes, V., Semiao, V. and Pinho, M.N.D. (2002). "The effect on mass transfer of momentum and concentration boundary layers at the entrance region of a slit with a nanofiltration membrane wall", *Chem. Eng. Sci.*, **57**(5), 735-748.

Karode, S. K. (2001). "Laminar flow in channels with porous walls, revisited", *J. Membrane Sci.*, **191**(1-2), 237-241.

Kim, S. and Hoek, E.M.V. (2005), "Modeling concentration polarization in reverse osmosis processes", *Desalination*, **186**(1-3), 111-128.

Kiso, Y., Kon, T., Kitaob, T. and Nishimura, K. (2001), "Rejection properties of alkyl phthalates with nanofiltration membranes", *J. Membrane Sci.*, **182**(1-2), 205-214.

Kiso, Y., Muroshige, K., Oguchia, T., Hiroseb. M., Oharab, T. and Shintani, T. (2011), "Pore radius estimation based on organic solute molecular shape and effects of pressure on pore radius for a reverse osmosis membrane", *J. Membrane Sci.*, **369**(1-2), 290-298.

Kiso, Y., Muroshige, K., Oguchia, T., Hiroseb. M., Oharab, T. and Shintani, T. (2010), "Effect of molecular shape on rejection of uncharged organic compounds by nanofiltration membranes and on calculated pore radii", *J. Membrane Sci.*, **358**(1-2), 101-113.

Mulder, M. (1991), *Basic principles of membrane technology*, Dordrecht, Netherlands, Kluwer Academic.

Porter, M. C., Ed. (1990), *Handbook of industrial membrane technology*, New Jersey, Noyes Publications.

Schausberger, P., Norazman, N., Chenb, V. and Friedl, A. (2009), "Simulation of protein ultrafiltration using CFD: Comparison of concentration polarisation and fouling effects with filtration and protein adsorption experiments", *J. Membrane Sci.*, **337**(1-2), 1-8.

Wijmans, J.G., Nakao, S., Van Den Berg, J.W.A., Troelstra, F.R. and Smolders, C.A. (1985), "Hydrodynamic resistance of concentration polarization boundary layers in ultrafiltration", *J. Membrane Sci.*, **22**(1), 117-135.

Wiley, D.E. and Fletcher, D.F. (2002), "Computational fluid dynamics modelling of flow and permeation for pressure-driven membrane processes", *Desalination*, **145**(1-3), 183-186.

Wiley, D.E. and Fletcher, D.F. (2003), "Techniques for computational fluid dynamics modelling of flow in membrane channels", *J. Membrane Sci.*, **211**(1), 127-137.

CC

Nomenclature

A_k	membrane porosity
c_i	concentration of solute i in the pore (mol m^{-3})
$C_{i,B}$	bulk concentration of solute i in the feed (mol m^{-3})
$C_{i,p}$	bulk concentration of solute i in the permeate (mol m^{-3})
$C_{i,W}$	concentration of solute i at the membrane surface (mol m^{-3})
D_i	diffusivity of the solute i in the bulk solution (m^2 s^{-1})
h	membrane channel half height (m)
j_i	flux of solute i (mol m^{-2} s^{-1})
J_V	volumetric flux (m^3 m^{-2} s^{-1})
$J_{V,approx}$	approximate volumetric flux used for initial rejection calculation (m^3 m^{-2} s^{-1})
$K_{i,c}$	hindrance factor for convection for solute i
$K_{i,d}$	hindrance factor for diffusion for solute i
L	membrane channel length (m)
L_S	solute length (m)
L_V	hydrodynamic permeability of the membrane (m Pa^{-1} s^{-1})
N_{Re}	entrance Reynolds number, $4u_0h\rho/\eta$
ΔP_{axial}	total axial pressure drop between the membrane inlet and outlet (Pa)
R_i	rejection of solute i
R_{cal}	predicted solute rejection
R_{obs}	experimentally determined solute rejection
r_p	pore radius (m)
S	area of smallest possible rectangle that fully encloses projection of solute onto plane perpendicular to axis coincident with line joining two most distant points on solute (m^2)
u_0	average inlet velocity (m s^{-1})
w	2D model artificial width (m)
W_S	solute width (m)
x	dimension in direction of axial flow across membrane surface
y	dimension in direction of pore flow through membrane
Δy	pore length (m)

Greek letters

η	viscosity of the water in the pore (Pa s)
Λ	osmotic pressure correction factor
Π_W	osmotic pressure at the membrane surface (Pa)
$\Delta\Pi_W$	osmotic pressure difference between the feed solution at the membrane surface and the permeate (Pa)
ρ	density of feed solution (kg m^{-3})
Φ	overall solute partition coefficient
ω_i	mass fraction of solute i
$\omega_{i,p}$	mass fraction of solute i in the permeate stream
$\omega_{i,W}$	mass fraction of solute i at the membrane surface